DISSERTATION

High Power Proton Beam Shocks and Magnetohydrodynamics in a Mercury Jet Target for a Neutrino Factory

ausgeführt zum Zwecke der Erlangung des akademischen Grades eines Doktors der technischen Wissenschaften unter der Leitung von

Ao. Univ. Prof. Dr. Christian W. Fabjan
E141
Atominstitut der österreichischen Universitäten

im Rahmen des

Austrian Doctoral Student Program

am CERN, CH-1211 Geneve 23

eingereicht an der Technischen Universität Wien

Fakultät für Technische Naturwissenschaften und Informatik

von

Dipl.Ing. Adrian Fabich

9226849

A-1060 Wien, Bürgerspitalgasse 9

Wien, im November 2002

Chapter 4

A Metal Jet in a High Magnetic Field

The US scenario for a neutrino factory foresees a solenoidal channel for pion capture (section 2.2.1). The high power target scheme relies on a mercury jet injected with a velocity of $\approx 30\,\mathrm{m/s}$ under an angle of 6 degree into the $20\,\mathrm{Tesla}$ magnetic field. A moving metal in an inhomogeneous field experiences forces caused by the change of the magnetic flux and the induced eddy currents. The magnetic field again acts on these eddy currents and results in magneto-hydrodynamic effects.
The layout in the region of interaction between proton beam and mercury jet is indicated in Figure 4.1. The target region is surrounded by the solenoidal channel (black square, indicated as shielding), where the minimum bore is $r = 7.5\,\mathrm{cm}$. The mercury jet is inclined by $100\,\mathrm{mrad}$ from the solenoid axis to maximise the pion yield. Table 4.1 summarises the geometrical parameters for the mercury jet and the proton beam [13]. A few meters downstream from the interaction region, the dispersed mercury is collected in a pool, which serves as the beam dump at the same time.
A mercury jet ($v \leq 15\,\mathrm{m/s}$, $d \approx 4\,\mathrm{mm}$) has been injected into a $20\,\mathrm{T}$ solenoid. The experimental conditions differ from the ones of the proposed neutrino factory and the purpose of these measurements is to benchmark the simulation tools for a full scale mercury jet target. In section 4.1 the experimental setup is described. This includes the solenoid configuration, the pump and the experimental chamber, where the jet is injected. Section 4.1.3 explains the diagnostics and the principle of measuring the properties of the jet. The results of the observation are presented in Section 4.2.

$\sigma_{proton\ beam}$	$1.5\,\mathrm{mm}$
α_{beam}	$-67\,\mathrm{mrad}$
β_{jet}	$-100\,\mathrm{mrad}$
$radius_{jet}$	$5\,\mathrm{mm}$
v_{jet}	$30\,\mathrm{m/s}$
jet material	mercury

Table 4.1: Geometric parameters of the proton beam and the mercury jet

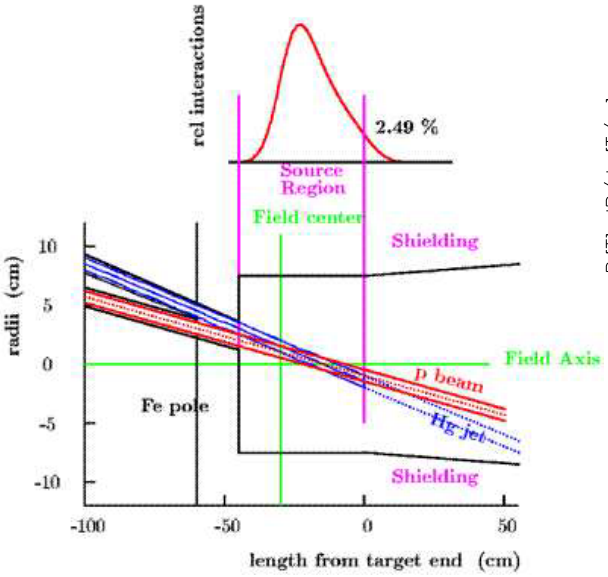

Figure 4.1: Layout of the US target scenario.

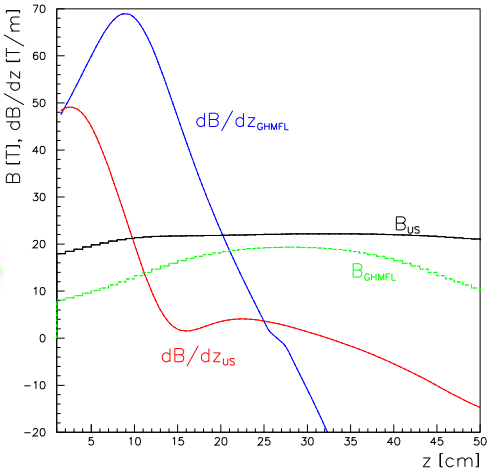

Figure 4.2: B-field of the M9 at Grenoble High Magnetic Field Laboratory (GHMFL) compared with the target section of the US-solenoid.

4.1 Experimental Layout

4.1.1 The 20 Tesla Solenoid M9

At the **G**renoble **H**igh **M**agnetic **F**ield **L**aboratory (GHMFL), M9 is a solenoid with a vertical bore of $d = 13\,\mathrm{cm}$ for the configuration, where the DC magnetic field can be ramped up to $\approx 20\,\mathrm{Tesla}$. Figure 4.2 shows the B-field of the solenoid M9 for magnetohydrodynamic studies at GHMFL and compares it with the one of the US decay channel. The maximum field is comparable, but its gradient is much higher in the case of M9. The bore can be accessed from the top. The bottom is closed at $44\,\mathrm{cm}$ below the maximum of the magnetic field, where the bore is reduced to $d = 5.5\,\mathrm{cm}$ over the last $17\,\mathrm{cm}$ (Figure 4.3).

4.1.2 The Jet Setup

The mercury jet is driven via a compressed air driven double piston pump feeding a nozzle placed in the magnetic field. A picture of the setup installed at GHMFL is shown in Figure B.1, where on the left hand side the pump rack is located. The blue confinement hose points towards the top of the experimental chamber, which is inserted in the vertical solenoid.

A flow chart of the setup is indicated in Figure B.2. A two stroke piston pump, which is air driven with a translation of $1/16$, accelerates the mercury. A detailed description of the pump NORDSON 25B, which is a commercial product for paint spray systems, can be found in [49]. It is neither designed for high flow rates nor to be used with mercury. The maximum air pressure of $6\,\mathrm{bar}$, limited by a safety valve, results in a static pressure of $90\,\mathrm{bar}$ on the mercury. The

tungsten seats of the ceramic ball valves broke regularly after typically 150 strokes [54], what forced dismantling of the mercury circuit to access and repair the pump. A detailed description of the gas rack, the mercury recuperation system and the handling procedures are given in [55]. A piezo-electric pressure gauge (Dytran 2300V5 pressure gauge) is mounted at the beginning of the high-pressure piping to monitor the dynamic pressure losses of the moving mercury.

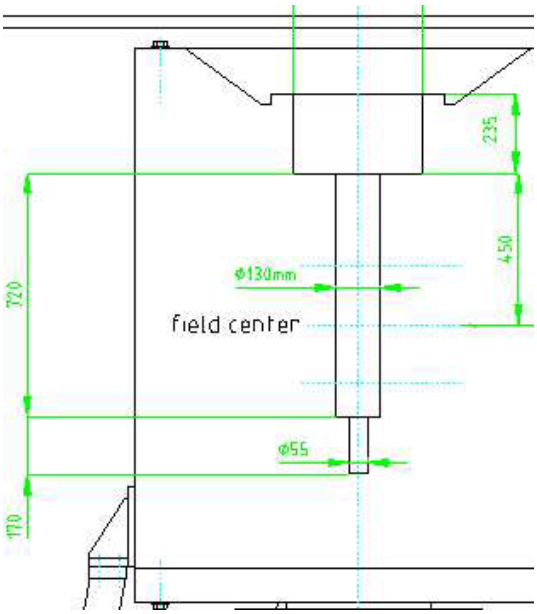

Figure 4.3: Technical drawing of the solenoid M9 at GHMFL

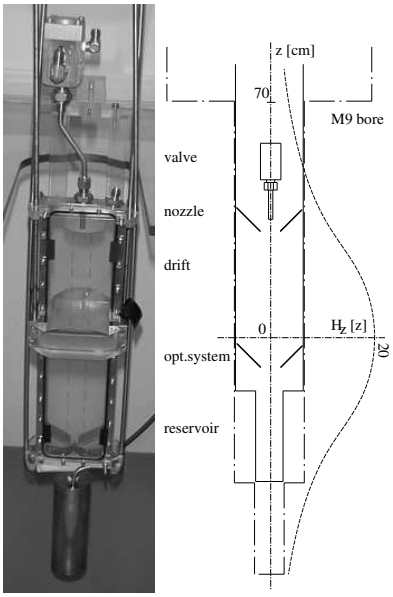

Figure 4.4: left: jet chamber; right: schematic in the bore of M9

Via the blue hose, containing gas and mercury supply, the pump rack is connected to the experimental chamber, which consists of an outer confinement containing the jet chamber (Figure 4.4). The shape of this outer steel tube is following the bore of the solenoid (see Section 4.1.1) and its cross-section is indicated in the following figures.

The Jet Chamber

Due to the working principle of the pump and due to the restricted space inside the experimental chamber and its reservoir, the mercury jet is pulsed. Spilled mercury can not be withdrawn from the chamber permanently and would block the observation view. An air-actuated ball valve, located next to the nozzle, allows to run the jet for an adjustable delay, typically of $100\,\mathrm{ms}$ (Figure 4.4). On triggering the valve, a mercury jet is ejected from the nozzle ($d_{inner} = 4\,\mathrm{mm}$) into the jet chamber, where it travels along a free path of $\approx 27\,\mathrm{cm}$. The jet chamber consists of a steel frame with a Makrolon cover on each side. At the bottom of the jet chamber splash guards in v-form collect the mercury and guide it into the cylindrical reservoir located below. With argon pumping of a few atmospheres the mercury can be recuperated to the main reservoir in the pump rack. The jet chamber with its double confinement is fixed to an elevator in order to vary its height. The position of the nozzles are chosen such, that the drift of the jet is either placed in the

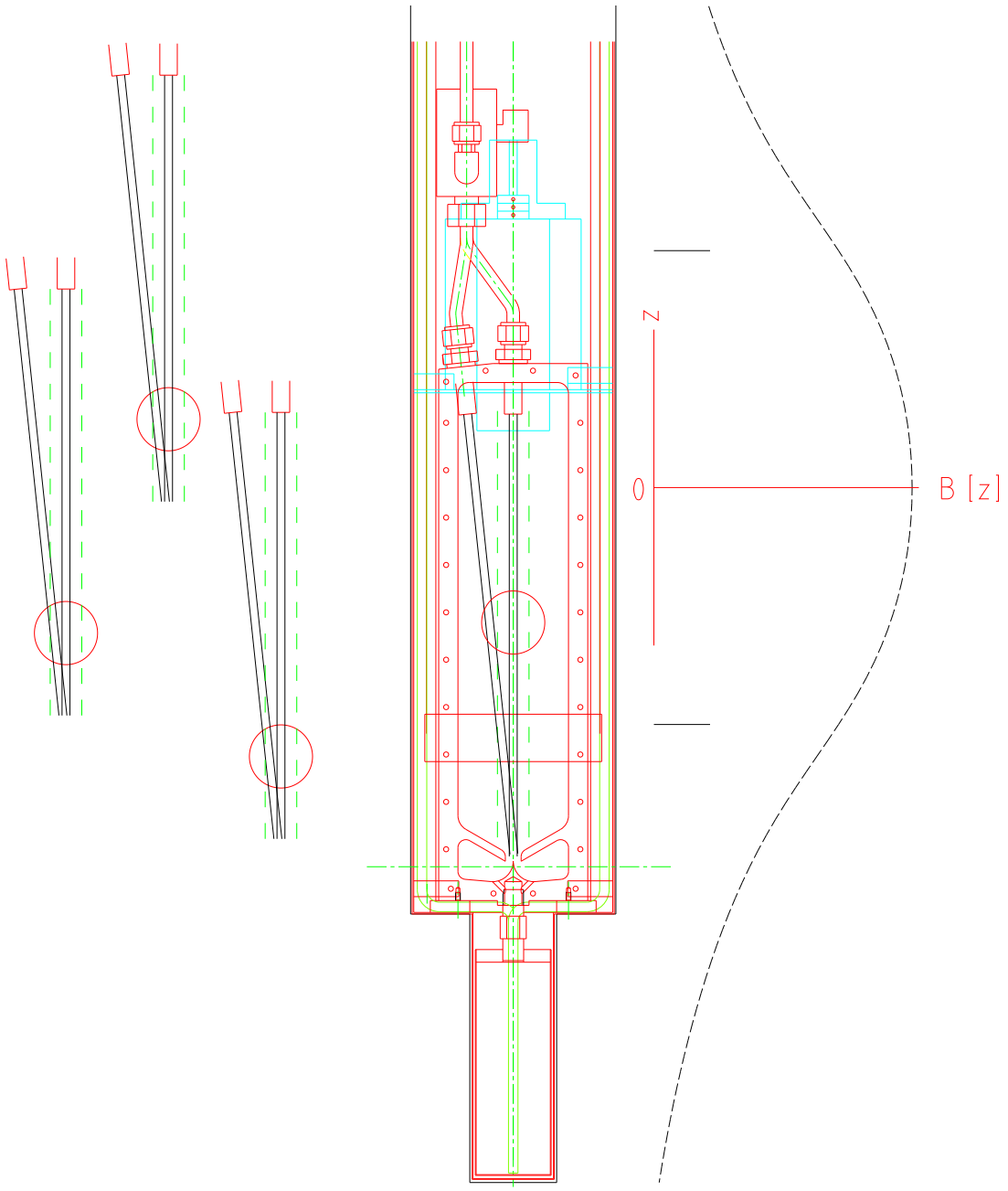

Figure 4.5: Short nozzles: collinear and tilted. Technical drawing of the jet chamber placed in the M9 bore with the nozzle at two different angles and at different positions indicated. The position 'lowest' is limited by the magnet bore, which is closed at the bottom.

positive or negative gradient, or in the maximum field (Figure 4.5). The chamber is filled with one atmosphere of argon normally, but an under-pressure can be applied. If not stated differently, the jet chamber was filled with one atmosphere argon.

The Nozzles

The connection of the nozzle is modular in such a way that various nozzles with different lengths and angles can be mounted. The nozzles differ in the length, which is measured from the valve until the outlet, and in the inclination, at which they are installed. Nozzles installed at two different angles ($0\,^{\circ}$ and $6\,^{\circ}$) are indicated in Figure 4.5. The figures on the left side show the possibility to move the drift path in respect to the magnetic field, which is shown on the right side. The left figures show besides the nozzle and the jet also the calibration grid (green dashed line) and a typical view area (red circle). Such nozzles with a short length ($\approx 13\,\mathrm{cm}$) are called “short”. The length of the nozzle is measured from the air-actuated valve to the tip of the nozzle. The left figures show only the tip of the nozzle, the full nozzle is indicated in the centred figure. Nozzles, where the tube length is extended to $\approx 23\,\mathrm{cm}$, are called long nozzles, where the longer pipe implies a accordingly shorter drift path as the position of the valve is fixed in respect to the experimental chamber as indicated in Figure 4.6. The different length of the nozzles produces a mercury jet with different properties (Section 4.2.3- 4.2.4).

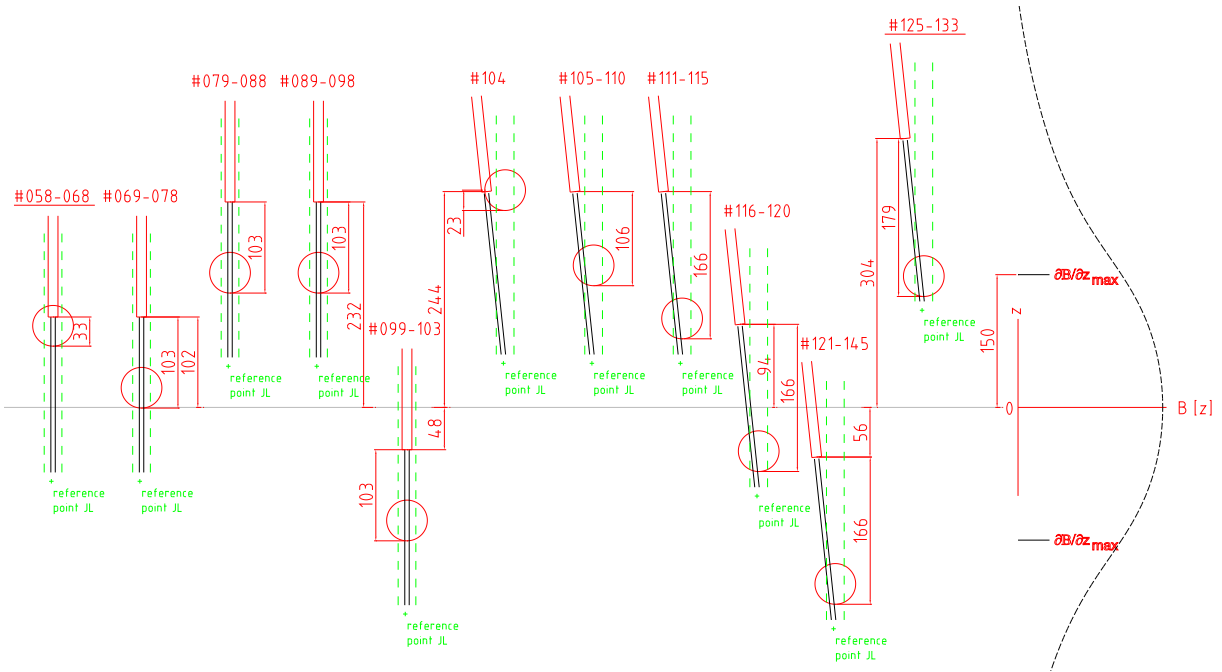

Figure 4.6: Positions of the long nozzles (straight/tilted) and the viewing area (circles) relatively to the solenoid for each set of data. The event indices are indicated.

4.1.3 Diagnostics and Digital Image Processing

As for the experiments on proton induced shocks, the MHD jet setup is based on the recording of the shadow of the mercury, intercepting a laser light source, with a high speed camera. Sets of mirrors allow the installation of the sensitive pieces of electronics outside of the magnetic field.

The light source is a laser diode, $35\,\mathrm{mW}$, $670\,\mathrm{nm}$, coupled to a few meter long fibre. The fibre guides the light into the confinement of the jet chamber. An optical lens focuses the light to a parallel beam with a diameter of $\approx 45\,\mathrm{mm}$. The stainless steel chamber equipped with transparent windows sits between two mirrors placed at 90 degree. The light is guided parallel to the jet, reflected via a plane mirror (Figure 4.4) by $90\,^{\circ}$ trough the Makrolon window, intercepts with the drift path of the jet and is again reflected by $90\,^{\circ}$ through the top of the confinement towards the high speed camera (Section 3.3.4). The optics allowed the observation of a $\approx 4\,\mathrm{cm}$ diameter surface movable along the field axis over a distance of 20 cm. The camera settings were $2000\,\mathrm{frames/second}$ for the recording rate and $25\,\mu\mathrm{s}$ for the shutter time. A typical view in absence of the mercury jet is shown in Figure 4.7. In Figure B.3 and B.4 a full image of the mercury jet can be seen, where the outer confinement was removed to directly view the drift path.

The digital image processing is similar to the case of the proton induced shocks (Section 3.3.4). The calibration and the random tilt of the central axis are corrected using the calibration grid (two parallel lines with a distance of 2 cm, each dashed $1\,\mathrm{cm}$ equidistant). The tilt correction and the extraction of the resolution (typically $0.33\,\mathrm{mm/pixel}$) is illustrated in Figure 4.7. The mercury jet was extracted by differential comparison with the initial frame. The raw jet, which is corrected for background, is indicated in Figure 4.8. The digital image processing allows to extract information like jet width, velocity and inclination, which is correlated with the offset. As the representative velocity for an event, the initial $50\,\mathrm{ms}$ of the fully established jet are averaged, except if clearly indicated velocity of the jet tip. The width and the inclination are averaged over $\approx 50\,\mathrm{ms}$ as well. The resolution of the camera and the typical length ($3\,\mathrm{cm}$) results a in a measurement error of approx. $\pm 5\%$ of the velocity.

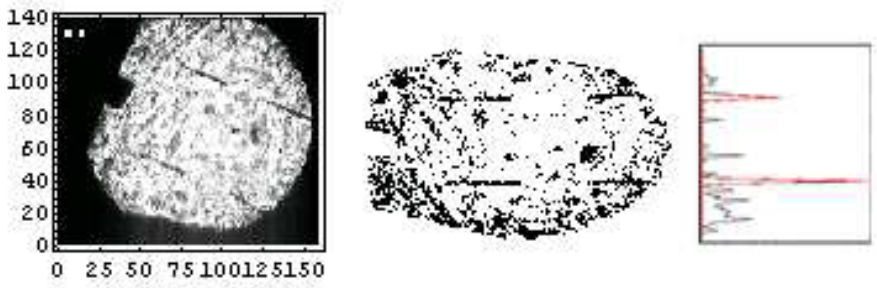

Figure 4.7: Extracting the calibration grid. From the original frame the black border is removed. A rotation and projection reveals the position of the calibration grid (two black, $1\,\mathrm{cm}$-dashed lines at a distance of $2\,\mathrm{cm}$). The resolution was typically $0.33\,\mathrm{mm/pixel}$ for the MHD experiment. In the left figure the tip of the nozzle is seen.

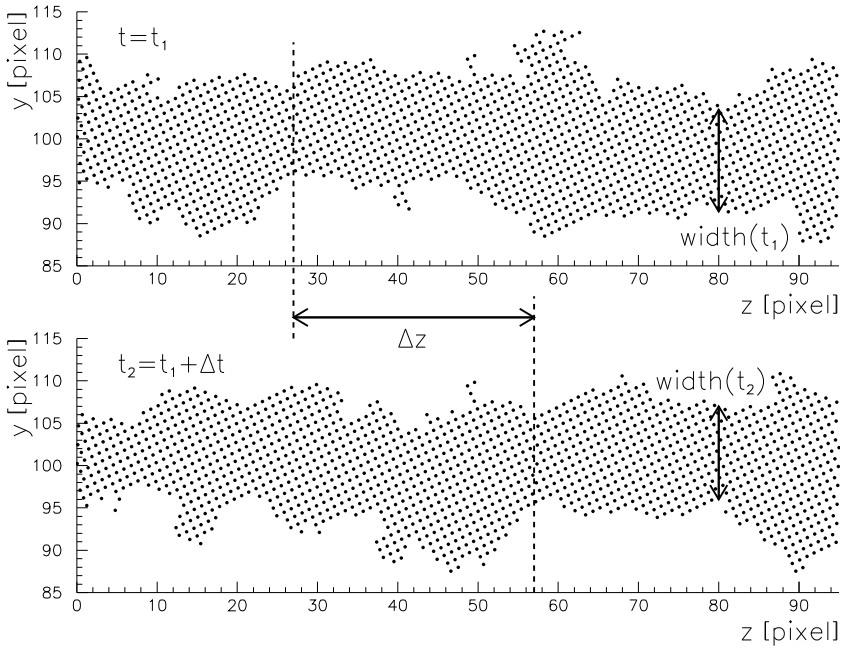

Figure 4.8: Width and velocity of a jet. From each frame the jet is extracted. The shape can be measured and reveals the width of the jet. The comparison of the jet shape from frame to frame reveals the shift per frame and the velocity $v = \frac{\Delta z}{\Delta t}$ can be calculated.

4.2 Observations

From the nozzle the jet is ejected with a velocity in absence of a magnetic field depending on the driving pressure as discussed in Section 4.2.1. The stabilising effect of the magnetic field on a turbulent (Section 4.2.3) and a quasi-stable (Section 4.2.4) jet are observed by using different nozzle types. The impact of the presence of a magnetic field on deflection, width and velocity are discussed in Section 4.2.6-4.2.8. Finally we compare with analytical calculations and numerical simulations, and conclude on the impact of the design for a full scale mercury jet in a magnetic field as foreseen for a neutrino factory.

4.2.1 Jet Velocity at B=0 T

The optical observation of the shape and the resulting determination of the velocity are presented in Figure 4.8 and 4.9. From each frame the position of both jet edges is measured. The difference of these two provides the width of the jet. Independent superposition of these three arrays (upper edge, lower edge, width) of two subsequent frames and the evaluation of the minimum difference by shifting along the jet axis gives the velocity $\mathrm{v} = \mathrm{shift} * \mathrm{rate}_{\mathrm{frame}}$.
Possible standing pressure waves could fudge the velocity measurement. That is excluded by independent analysis of the three arrays. Additionally the measurement of obvious mass movements, like tip and tail of the jet, have been determined manually and agree with the results of the digital analysis. In Figure 4.9 the jet velocity for a representative event is plotted as a function of time.

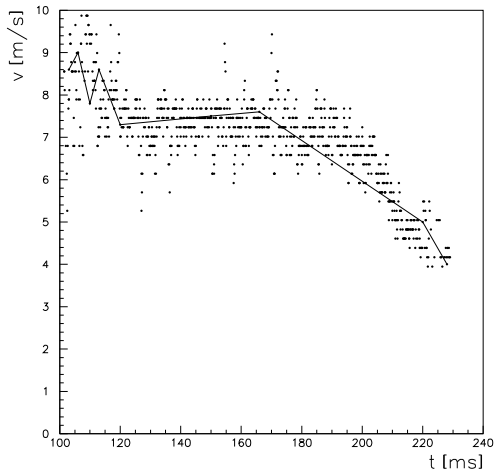

Figure 4.9: Velocity of the jet as a function of time. The digital retrieved data (points) corresponds to the measurement of obvious jet movement analysed manually (line).

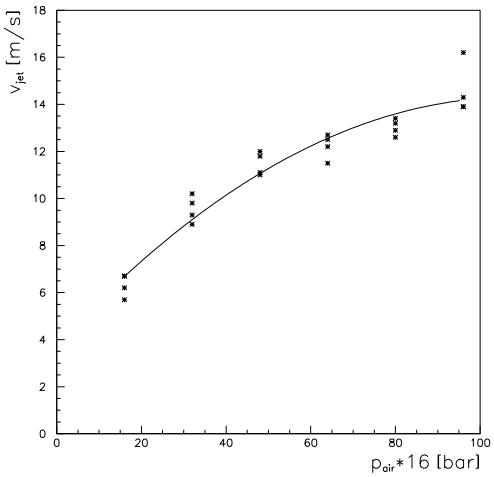

Figure 4.10: Jet velocity as a function of the driving pressure.

The jet velocity as a function of the air pressure in the pump is indicated in Figure 4.10, obtained from calibration measurements without magnetic field. With a trigger gate of $100\,\mathrm{ms}$ of the air actuated valve the corresponding jet length is in the order of $1\,\mathrm{m}$. For low velocities the gate was prolonged to keep the length several times above the drift length.

Jet in the Evacuated Chamber

Normally the jet was injected in one atmosphere Argon. Applying a pressure of a few Torr in the jet chamber showed negligible change in the width. After a drift path of $10.3\,\mathrm{cm}$ at low pressure the average width at $2\,\mathrm{bar}$ driving pressure measured as $w = 4.1\,\mathrm{mm}$, $w = 4.2\,\mathrm{mm}$ in atmosphere. At $4\,\mathrm{bar}$ driving pressure the width changed to $5.1\,\mathrm{mm}$ and $5.2\,\mathrm{mm}$ respectively. The jet velocity at low pressure in the chamber corresponds to the one if the chamber is filled with argon (Figure 4.10).

4.2.2 Dynamic Pressure

The piezo-sensor records the dynamic pressure losses in the high pressure hose (Figure 4.11). With a typical delay of $60 - 90\,\mathrm{ms}$ after the trigger the pressure drops. This is caused by the filling of the air supply to the air-actuated valve and the opening of the pneumatic valve itself. The delay of valve opening is related to the strength of the magnetic field. The jet passes with an additional delay to reach the view area. From this time ($100 - 140\,\mathrm{ms}$) onwards the velocity data are indicated (Figure 4.11). The trigger gate ends after $100\,\mathrm{ms}$. The pressure drop gets smaller with the magnetic field. This indicates a resistive force on the ball valve and/or the mercury in the pipe.

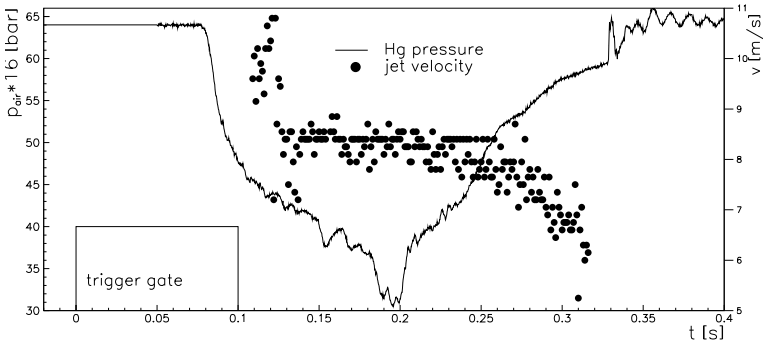

Figure 4.11: Pressure in the mercury supply and the jet velocity as a function of time. The pressure loss is recorded with the piezo-gauge. The velocity is digitally retrieved from the movies.

4.2.3 The Sprayed Jet

The two types of nozzle produced two different kind of jets. From the 'short' nozzle the jet could not evolve properly and the jet looks more like a 'cloud' of mercury ('sprayed' jet).
Figure 4.12 shows the sprayed jet in the absence and presence of a magnetic field. The Jet could not be stabilised by the magnetic field, independently of the inclination and the position of the nozzle referred to the magnetic field. The frames are such chaotic that a digitally analysis is impossible (with reasonable effort). The number of small single droplets is reduced in the case of magnetic field presence. Clearly visible is the effect of the repulsive force by the magnetic field, where the droplets tend to smooth and are stretched in backward direction. Also, the velocity of the jet is reduced similar to the observation in the case of the 'stable' jet (Section 4.2.4).

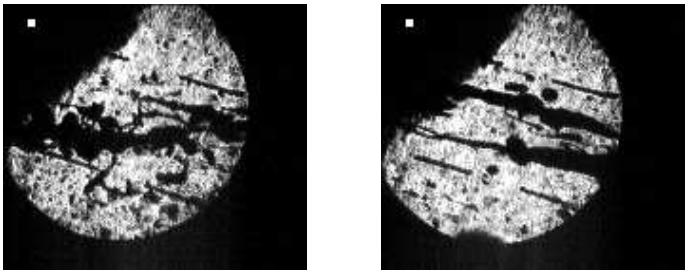

Figure 4.12: The sprayed jet without (left) and in a magnetic field (right). The jet arrives from the left hand side.

4.2.4 The Stable Jet

With the 'long' nozzle a different type of jet, a 'stable' jet was obtained. Single frames from the film of the 'stable' jet injected under 6 degree are presented in Figure 4.13. The tip of the jet and the jet itself recorded 10 ms after the passage of the tip are given for injection velocities between 8 and $12\,\mathrm{m/s}$ and a field strength up to $19.3\,\mathrm{Tesla}$. With increasing field, the smoothness of the jet envelope is clearly improved thus demonstrating the expected damping. The results presented in Section 4.2.5-4.2.8 are obtained with running a 'stable' jet.

4.2.5 The Jet Tip

A $4\,\mathrm{mm}$ diameter jet injected in a 20 Tesla field stabilised at the desired injection angle within 10 ms (Figure 4.14). Minor misalignments or oscillation around the axis of the jet cannot be excluded.The first figure shows the jet width for a jet without magnetic field. At $19\,\mathrm{T}$ the tip is more pointed. The width of the jet is fully established at $t < 10\,\mathrm{ms}$. The time is reset to zero at the first indication of the jet, thus correcting for the time delay caused by the air actuated valve in a magnetic field. Clearly seen in Figure 4.14 is the damping of the surface oscillations: Larger fluctuations of the width are suppressed by the magnetic field.

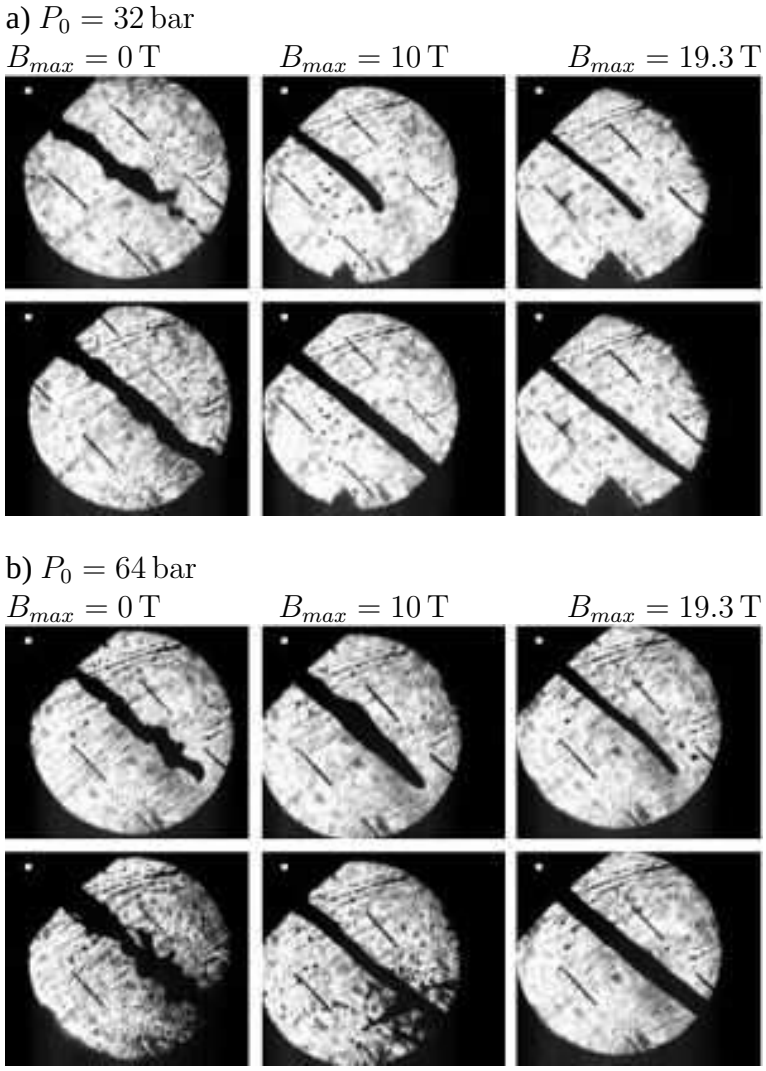

Figure 4.13: Mercury jet injected at 6 degree into the bore of the M9 magnet at GHMFL Grenoble. The tip of the jet is presented in the top row and the second row is a snap shot of the jet taken 10 ms after the passage of the tip. The static pressures driving the mercury were 32 (a) and 64 bars (b)

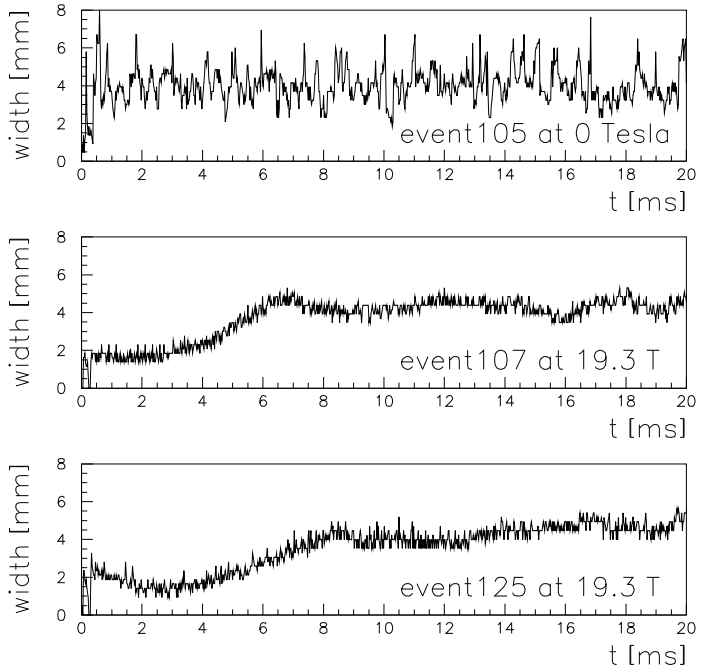

Figure 4.14: The width of the jet as a function of time at $0\,\mathrm{T}$ and $19.3\,\mathrm{T}$. A clear smoothing of the jet shape at $19.3\,\mathrm{T}$ is visible.

4.2.6 Deflection

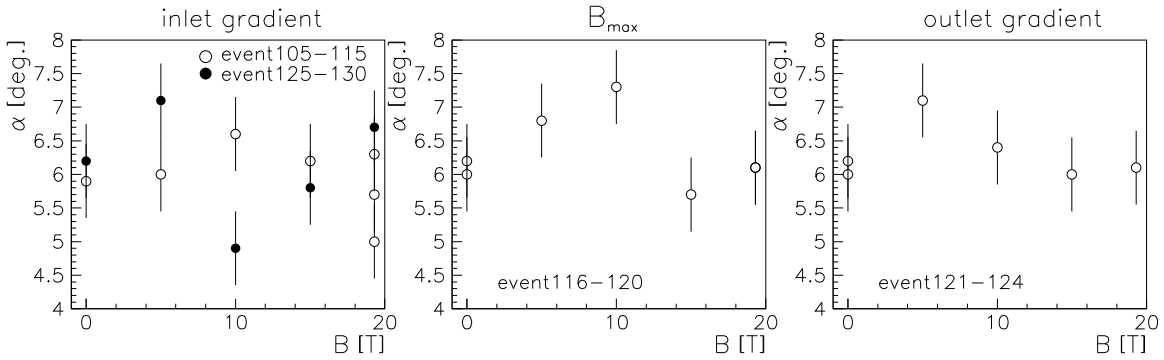

Figure 4.15: Deflection as a function of the magnetic field for several positions of the drift path as given in Figure 4.6.

The injection of the inclined jet showed no deflection of the jet. In Figure 4.15 the inclination of the jet is plotted for a drift path through the positive gradient (event 105-115 and 125-130), through the maximum field (event 116-120) and out of the magnetic field (event 121-124). The error indicated originates from the uncertainty given by the resolution of the camera. The angle is defined as the inclination between jet and solenoid axis.

4.2.7 Jet Diameter

The jet diameter was studied as a function of the position of the jet in the magnetic field. The diameter has a general tendency to decrease with increasing magnetic field (Figure 4.16-4.18). The typical width decrease is about 10% for the injection of a collinear jet. In Figures 4.16 and 4.17 the width for the jet on entering the magnetic field is shown for two different distances of observation from the tip of the nozzle.
A large effect is seen (Figure 4.18, open circles), where the drift path is in the negative gradient after the maximum field. A width decrease of about 30% is measured. This indicates the occurrence of MHD effects in the pipe itself. The width of the jet on traversing the positive gradient, implying the position of the valve and nozzle in a comparable low magnetic field and gradient, is constant as indicated in Figure 4.18. The MHD effects of the confined flow of the mercury in the valve and the nozzle are subject to further investigations.
For the tilted injection at 6° the change in width can result in a deformation of the cross section of the jet. The tilted injection makes the problem asymmetric in respect to the magnetic axis and could cause a broadening in the view axis. However, this effect could not be analysed with our diagnostics.

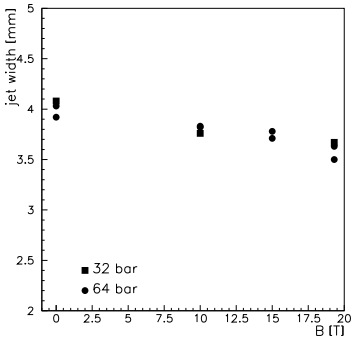

Figure 4.16: Pinching for the straight jet on traversing the field maximum measured at a distance $d = 3.3\,\mathrm{cm}$.

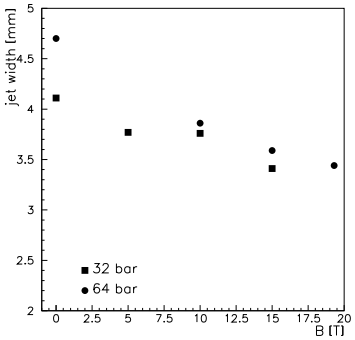

Figure 4.17: Pinching for the straight jet on traversing the field maximum measured at $d = 10.3\,\mathrm{cm}$.

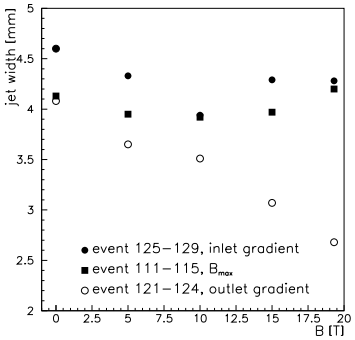

Figure 4.18: Pinching of the inclined jet.

4.2.8 Velocity

The velocity measurement relies on the shift of the jet shadow. This implies that the velocity measured is the one of the surface only. Figure 4.13 shows samples of the fully established jet. At high magnetic field the surface oscillations are damped and the amplitude is comparable to the resolution. This effect results in difficulties to determine precisely the velocities at high magnetic field. Approaches by different diagnostics are mentioned in the conclusions. Overall the velocity decreases with the magnetic field (Figure 4.19). The tip of the jet has a lower velocity than the fully established jet.
Jet velocities are presented in Figure 4.19 as a function of the magnetic field strength for different initial pump pressure and injection angles. The expected tendency for the velocity of the jet to be reduced with increasing field is observed. Independent of the injection angle the velocity is about 25% less at highest magnetic field.

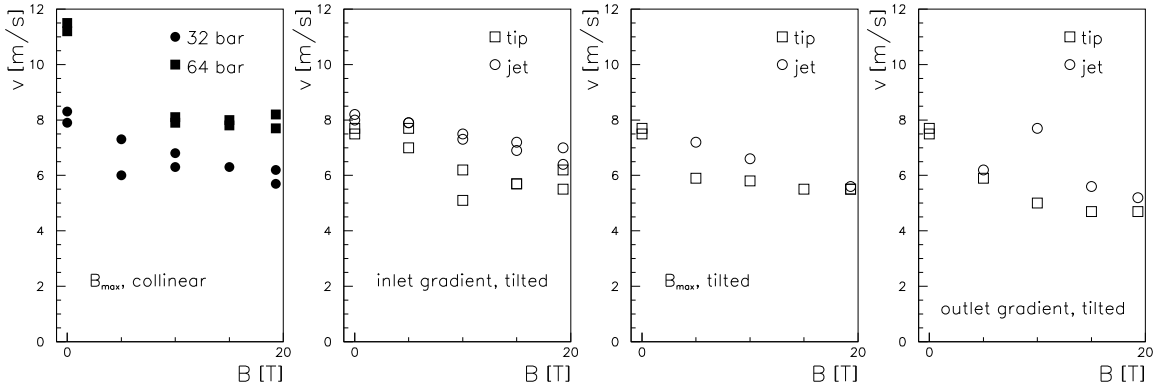

Figure 4.19: Jet velocity versus magnetic field

Appendix B

The mercury jet setup for the MHD experiment

Figure B.1: The experimental setup at GHMFL M9. The vertical bore of the solenoid is lowered in the floor, where the blue hose is pointing to. To the other end the pump device is connected. On the left hand side the gas rack can be seen.

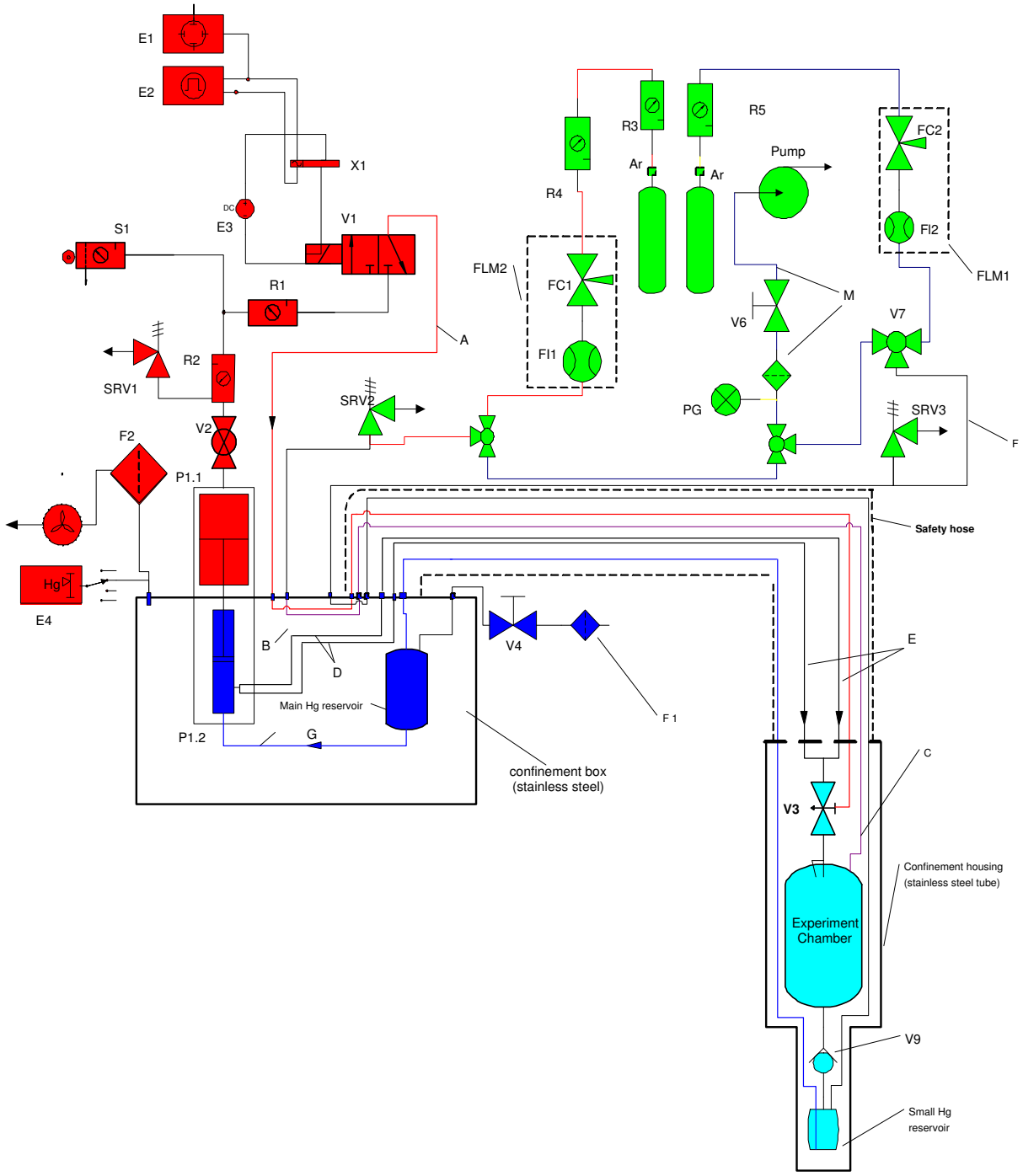

Figure B.2: Flowchart of the mercury pump system for the MHD jet setup (legend see Table B.1)

index	description
E1	Oscilloscope Tektronix TDS3032 300Mhz, 2.5Gs/s
E2	Pulse Generator Philips/Fluke PM5786B 1Hz-125MHz
E3	Power Supply 24V DC
E4	Mercury Vapor Detector Mercury Instruments VM-3000
F1, F2	Charcoal Filter
FLM1,FLM2	Flow meter Vögtlin Q80EE S1 M12G A2.0E
FC1	Flow Control for Noble Gas
FC2	Flow Control for Noble Gas/Air
FI1,FI2	Flow Indicator (Flow meter) 0-10 l/min
PG	Pressure gauge for under-pressure
P1.1	NORDSON 25B Piston Pump, Air Motor
P1.2	NORDSON 25B Piston Pump, Hydraulic Section
P3	Rotary pump
R1	Air Pressure Regulator
R2	Air Pressure Regulator
R3	Pressure Regulator for Argon LHC15 200bar→15bar
R4	Pressure Regulator for Argon BS300/01 15bar→10-100 mbar
R5	Pressure Regulator for Argon and Air
S1	Air Service Station (Filter, Pressure Regulator)
V1	3/2 Pneumatic Valve
V2	Shut Off Valve for Air Motor of Piston Pump
V3	NORDSON A7A Ball Tip Valve (air actuated)
V4	Screw down valve
V5	Pneumatic valve / non return
V6	Screw down valve
V7	Mixing valve
V8	Three way valve
V9	One way valve
SRV1	Safety Relief Valve 4.1 bar
SRV2,SRV3	Safety Relief Valve “Nupro”, 0,2-3bar (calibrated to 0,2bar)
X1	Reed Relays 5V
	Tube and hose types, contained medium
A	4x6mm Rilsan (Polyamide) flexible hose; medium: compressed air
B	5x6mm stainless steel tube; medium: compressed air
C	4x6mm Rilsan (Polyamide) flexible hose; medium: compressed air
D	6x8mm stainless steel tube; medium: mercury (high pressure)
E	2x NORDSON high-pressure hoses, Teflon 1/4”, stainless steel nipples and swivel nuts; medium: mercury (high pressure)
F	6x8mm stainless steel tube; medium: compressed air
G	1/2” plumbing (316 stainless steel); medium: mercury
I	6x8mm stainless steel tube; medium: air
L	1/2” plumbing (316 stainless steel); medium: mercury
M	4x6mm Rilsan (Polyamide) flexible hose; medium: compressed air
	Feedthrough fittings: Gyrolok, stainless steel

Table B.1: Components of the mercury pump system for the MHD jet setup

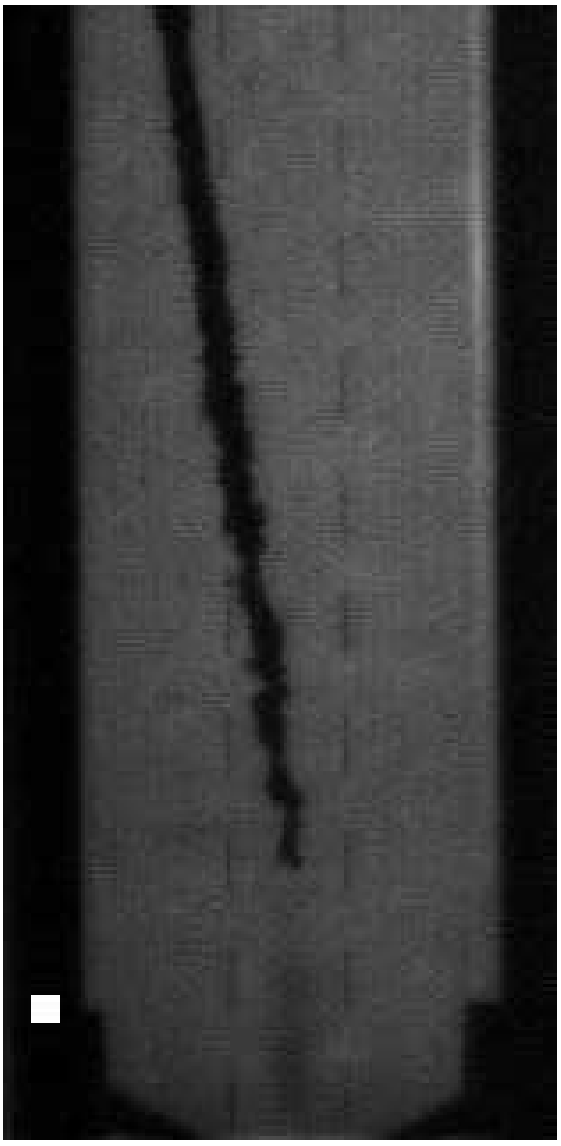

Figure B.3: A full view of the MHD jet ($64\,\mathrm{bar}$, long nozzle at $6\,\mathrm{degree}$) at $11\,\mathrm{ms}$ and ...

Figure B.4: ... $76\,\mathrm{ms}$ after ejected from the nozzle. The splashing of the mercury in backward direction along the steel frame can be seen.